Chemical Science

EDGE ARTICLE

View Article Online
View Journal | View Issue

Cite this: *Chem. Sci.*, 2015, **6**, 3965

Chemical looping of metal nitride catalysts: low-pressure ammonia synthesis for energy storage†

R. Michalsky,*[abc] A. M. Avram,‡[a] B. A. Peterson,§[a] P. H. Pfromm[a] and A. A. Peterson[b]

Received 4th March 2015
Accepted 28th April 2015

DOI: 10.1039/c5sc00789e

www.rsc.org/chemicalscience

The activity of many heterogeneous catalysts is limited by strong correlations between activation energies and adsorption energies of reaction intermediates. Although the reaction is thermodynamically favourable at ambient temperature and pressure, the catalytic synthesis of ammonia (NH_3), a fertilizer and chemical fuel, from N_2 and H_2 requires some of the most extreme conditions of the chemical industry. We demonstrate how ammonia can be produced at ambient pressure from air, water, and concentrated sunlight as renewable source of process heat *via* nitrogen reduction with a looped metal nitride, followed by separate hydrogenation of the lattice nitrogen into ammonia. Separating ammonia synthesis into two reaction steps introduces an additional degree of freedom when designing catalysts with desirable activation and adsorption energies. We discuss the hydrogenation of alkali and alkaline earth metal nitrides and the reduction of transition metal nitrides to outline a promoting role of lattice hydrogen in ammonia evolution. This is rationalized *via* electronic structure calculations with the activity of nitrogen vacancies controlling the redox-intercalation of hydrogen and the formation and hydrogenation of adsorbed nitrogen species. The predicted trends are confirmed experimentally with evolution of 56.3, 80.7, and 128 μmol NH_3 per mol metal per min at 1 bar and above 550 °C *via* reduction of $Mn_6N_{2.58}$ to Mn_4N and hydrogenation of Ca_3N_2 and Sr_2N to Ca_2NH and SrH_2, respectively.

1. Introduction

Ammonia is one of the most important synthetic chemicals in today's economy. With an annual production of about 162 million metric tons,[1] NH_3 is irreplaceable as a fertilizer, responsible for growing the food for approximately half of the world's population.[2,3] However, the catalytic synthesis of NH_3 from N_2 and H_2 is realized at some of the most severe process conditions of the chemical industry, *i.e.*, about 300 bar and 400–500 °C (ref. 4 and 5) (the Haber–Bosch process), and consumes energy at 28–166 GJ per ton NH_3 (ref. 1 and 5) in the form of natural gas, coal, or Naphtha;[1] this is 1–2% of the world's annual energy production.[6] About 15% of these net energy requirements are consumed for the technologically sophisticated high-pressure operations alone.[1] The fossil-fuel dependence links food security to natural gas price fluctuations and results in net CO_2 emissions of 1.9 tons (H_2 generation *via* steam reforming of natural gas) to 16.7 tons (H_2 generation *via* partial oxidation of coal) per ton NH_3.[1] Economies of scale dictate the need for large facilities producing typically 1000–3000 tons NH_3 per day,[1] which requires a highly developed infrastructure for production and distribution.[2] The conceivable development of a catalyst for a low-pressure and low-temperature Haber–Bosch process could theoretically alleviate these conditions. Although thermodynamically favorable at ambient temperature and pressure, no catalyst has been found that establishes reasonable reaction rates at these conditions,[7] which has been rationalized with the scaling of the activation energy for the N_2 dissociation and the adsorption energy of nitrogen at the catalyst surface.[7–9]

Beyond its irreplaceable use in agriculture, the use of NH_3 as a fuel is an attractive proposition since it is easily liquefied, rendering it a stable one-way hydrogen carrier and one of the most energy-dense zero-carbon fuels[10,11] that can be used as a direct substitute for fossil fuels in internal combustion engines.[12] This, and the prospect of zero-CO_2-emission vehicles, have motivated the development of the "AmVeh" car prototype

[a]*Department of Chemical Engineering, Kansas State University, 1005 Durland Hall, Manhattan, Kansas 66506, USA. E-mail: michalskyr@ethz.ch; Tel: +41-44-6338383*

[b]*School of Engineering, Brown University, 184 Hope Street, Providence, Rhode Island 02912, USA*

[c]*Department of Mechanical and Process Engineering, ETH Zürich, 8092 Zürich, Switzerland*

† Electronic supplementary information (ESI) available: Experimental and computational details, free energy plots for the NH_3 evolution and N_2 reduction with Co_3N/Co, Fe_4N/Fe, Mn_5N_2/Mn_4N, Mo_2N/Mo, CrN/Cr_2N, TaN/Ta_2N, NbN/Nb_2N, Li_3N/LiH, Ba_3N_2/BaH_2, Sr_3N_2/SrH_2, and Ca_3N_2/CaH_2, surface oxidation energetics, $\Delta G_{vac}[NH_x^*, yH^*]$ based on gas phase H_2 as hydrogen source, NH_3 evolution with Fe-doped Mn_4N, NH_3 evolution with $Mn_6N_{2.58}$, Ca_3N_2 and Sr_2N after correcting for partial nitride hydrolysis, NH_3 yield from Ca_3N_2 *vs.* time and H_2 gas flow rate. See DOI: 10.1039/c5sc00789e

‡ Present address: College of Engineering, 4183 Bell Engineering Center, University of Arkansas, Fayetteville, Arkansas 72701, USA.

§ Present address: Department of Chemical and Biological Engineering, Missouri University of Science and Technology, 143 Schrenk Hall, Rolla, Missouri 65409, USA.

fueled by a 70% NH_3/30% gasoline blend.[13] Current combustion research is focused on increasing the energy substitution by NH_3 and improving the exhaust treatment for removing uncombusted NH_3.[13,14] Additionally, NH_3 can be used in alkaline fuel cells that decompose NH_3 into N_2 and H_2 fuel[15] for direct electricity generation.[16] The development of the electrocatalysts and the cell design are currently limiting the costs and efficiency of this technology.[16] The synthesis of ammonia as a "solar fuel",[17] could conceivably be deployed beginning with the electrolysis of water with photovoltaic electricity[18] (the generated H_2, however, would require massive investments into infrastructure for compression, storage and transport, hindering its direct use). Instead, H_2 could be employed for the synthesis of more practical liquid ammonia-based fuels *via* the conventional Haber–Bosch process. However, this technology requires sophisticated multi-step high-pressure and high-temperature unit operations and high-value electricity to operate these units due to the limited activity of the employed heterogeneous catalysts.[1,2,19]

One proposed means to circumvent the high-pressure and high-temperature requirements of the Haber–Bosch process is the electrochemical reduction of N_2 to synthesize NH_3 with solar-derived photovoltaic electricity at ambient pressure and temperature.[20–22] NH_3 evolution at the cathode becomes thermodynamically favorable at an equilibrium potential of 0.1 V *vs.* the reversible hydrogen electrode, RHE,[20,21] and electronic structure calculations have suggested materials may be found that would liberate NH_3 at about −0.5 V *vs.* RHE.[21,23,24] However, no suitable electrocatalyst has been identified experimentally for these potentials – the observed rates of NH_3 evolution are low and the best reported Faradaic efficiencies are in the order of 0.2–2%,[20,25] while more negative (stronger) potentials decrease the Faradaic efficiency further due to the competing hydrogen evolution reaction.

This article introduces an alternative approach: splitting of a catalytic reaction into two separate reaction steps that are facilitated with a looped metal compound catalyst. We demonstrate this approach with looped metal nitride catalysts for solar-driven low-pressure synthesis of ammonia. Solar-driven thermochemical N_2 reduction could circumvent the high-pressure requirements of the Haber–Bosch process and the energetic deficiencies of the electrochemical N_2 reduction. This approach separates the NH_3 synthesis into two reaction steps:[26–29] first, N_2 is reduced, typically, with a metal oxide and concentrated sunlight at elevated temperatures yielding a metal nitride. In a second step, the metal nitride is oxidized with H_2O to yield NH_3 and the restored metal oxide at lower temperatures. On paper, the optimization of the reactive materials[30,31] and of the solar radiation receiver-reactor technology[32] could allow us to approach solar-to-fuel energy conversion efficiencies of 70–75%, for solar radiation concentrated 5000-fold to 800–1500 °C.[33] However, while NH_3 can be formed at 1 bar and 200–500 °C by the oxidation of certain metal nitrides with H_2O,[27,34,35] recycling the metal oxide requires either a chemical reducing agent, such as biomass and/or syngas, or temperatures above 1500 °C.[26–29]

We propose production of NH_3 and O_2 from H_2O and N_2, without a sacrificial reducing agent and at moderate temperatures, *via* solar-driven cleavage of H_2O into H_2 and O_2 (ref. 30 and 31) and subsequent fixation and hydrogenation of N_2 with H_2 into NH_3 at 1 bar and up to 800 °C using a looped metal nitride catalyst and concentrated solar energy. Looped metal nitrides may decouple scaling of the nitrogen adsorption energy with the activation energy for N_2 dissociation that typically limits the activity of Haber–Bosch catalysts,[7] since the chemical potential of a metal nitride can be utilized in a low-temperature oxidation liberating NH_3, while N_2 can be reduced *via* recycling the metal nitride at elevated temperatures. At the process scale, this approach does neither require electricity for NH_3 formation nor the infrastructure for supplying natural gas or coal and the know-how and technology for high-pressure operations. As indicated by our previous net-present value analysis of solar-driven NH_3 synthesis *via* metal nitride hydrolysis,[26] such a process can be economically more attractive in geographically, economically, or politically isolated regions than NH_3 from large-scale Haber–Bosch plants.

In a broader context, looped nitride catalysis is analogous to looped oxide catalysis with reduced metal oxides that provide oxygen vacancies for the abstraction of oxygen from, for instance, bio-oils upgraded with H_2 into hydrocarbons.[36] Looped nitride catalysts provide active lattice nitrogen that is converted with H_2 into NH_3 and nitrogen vacancies, with ideally high selectivity for NH_3 and no formation of N_2 and N_2H_4. This is in contrast to the activity of redox materials, for instance, for solar-driven splitting of CO_2 and H_2O with total selectivity for CO, H_2, and O_2.[33,37] In turn, established computational tools for the rational design of heterogeneous catalysts and electrocatalysts, such as free energy minimization to determine reaction paths,[38,39] can be utilized to develop reducible metal nitride catalysts. In the following two Sections we employ electronic structure theory to determine and describe limiting reaction energetics for metal nitrides. Comparable to chemical looping applications, the oxygen vacancies of a looped oxide may be regenerated at high temperatures with concentrated solar energy, while the nitrogen vacancies of a looped nitride are refilled *via* solar-driven N_2 reduction. While we discuss trends in the bond strength of nitrogen adsorbates and lattice nitrogen, the presented principles are expected to apply analogously to the bond strength of oxygen, that governs the adsorption of oxygen at electrocatalysts for the oxygen reduction and evolution reactions (ORR/OER),[40,41] the reversible oxygen vacancy formation at metal oxide surfaces for selective deoxygenation,[42] and the oxygen exchange capacity of metal oxide redox materials for solar-driven CO_2 and H_2O splitting.[31,33,37,43] The discussed metal nitrides form a bridge between materials with weak metal–nitrogen bonds for nitrogen activation[44–46] and materials with strong metal–nitrogen bonds for hydrogen storage,[10,11,47,48] such as certain Li-based compounds which may reversibly release H_2 at reasonable pressures and temperatures (*e.g.*, 0.4–20 bar and 195–285 °C for Li_3N/Li_2NH)[47] and that ideally do not liberate NH_3.[49]

In this article we suggest design principles – which we derive from both electronic structure calculations and experiments – that can inform the design of a metal nitride for solar-driven ammonia synthesis. Section 2.1 outlines the ammonia-

synthesis potential of metal nitrides that facilitate the incorporation of hydrogen into the bulk crystal lattice. This is rationalized in Section 2.2 *via* electronic structure calculations that describe how nitrogen vacancies control NH_3 evolution at the atomic scale. Sections 2.3 and 2.4 quantify the reaction kinetics of NH_3 evolution and experimentally demonstrate the augmented conversion of lattice nitrogen *via* hydrogenation of metal nitrides relative to the reduction of metal nitrides.

2. Results and discussion

2.1 Thermochemical reactivity of metal nitride catalysts

We start by using literature data to provide basic reactivity principles for nitrides and to outline the pressure and temperature conditions of the proposed ammonia production *via* chemical looping of metal nitride catalysts. Similar to the Sabatier principle in catalysis,[7,21,45] producing NH_3 from N_2 and H_2 *via* looping of a metal nitride catalyst should have an optimum stability of the metal–nitrogen bond. At one extreme, thermally unstable nitrides – such as Co_3Mo_3N, Ni_3N, Cu_3N and Zn_3N_2 – have been shown to yield much NH_3 *via* denitridation with H_2 at about 250–400 °C.[44,46] However, the latter three materials are too unstable to be regenerated with N_2 at 1 bar[46] and a completely reversible recycling of Co_3Mo_3N from the formed Co_6Mo_6N requires long-time heating for 4 h in H_2/N_2.[44] On the other extreme, some more stable metal nitrides, when reacted with H_2, absorb hydrogen reversibly yielding mixtures of metal imide, amide and hydride (*e.g.*, Li_2NH, $LiNH_2$ and LiH from the reaction of Li_3N with H_2), rather than being selective to NH_3.[47,48] These nitrides can liberate some NH_3 at elevated temperatures in the presence of H_2, *e.g.*, from $LiNH_2$ above 300 °C (ref. 47) and from Ca_3N_2 above 600 °C.[50] Ideally, an intermediate metal–nitrogen bond strength would balance these effects.

In principle, the reduction of a metal nitride yields NH_3 and a lower nitride phase:

$$M_aN_b + \frac{3\delta}{2}H_2 \leftrightarrow M_aN_{b-\delta} + \delta NH_3 \quad (1)$$

where M represents a metal, a and b are stoichiometric constants and δ is the amount of lattice nitrogen extracted. The cycle can be closed if the solid is regenerated with N_2:

$$M_aN_{b-\delta} + \frac{\delta}{2}N_2 \leftrightarrow M_aN_b \quad (2)$$

Ideally, both reactions would have an exergonic region of temperature space, such that NH_3 is synthesized *via* a temperature-swing operation. Fig. 1A shows thermodynamic calculations of both reactions as functions of temperature for some representative systems. Unfortunately, none of these reactions exhibits this characteristic; instead, this figure generally identifies NH_3 evolution to be endergonic and N_2 reduction to be exergonic, except for Fe_4N and Co_3N (ESI†) with reversed reaction energetics. This can be understood due to the low thermal stability of Fe_4N and Co_3N.

To understand these trends, Fig. 2A shows the free energy of NH_3 evolution *vs.* the product of the number of d-electrons in the metal ground state, N_d, and the energy of these electrons, E_d. The analysis suggests increasing NH_3 evolution and decreasing stability of the metal–nitrogen bond with increasing occupancy of the d-states, which indicates their antibonding character. This phenomena is well known from the interaction of adsorbates at transition-metal surfaces.[52] While we did not include Ni_3N, Cu_3N and Zn_3N_2 in this analysis due to limited thermodynamic data, the high NH_3 yields with these unstable metal nitrides[46] can be understood due to an even higher number of d-electrons, relative to Fe_4N. We suggest that the trade-off between NH_3 evolution and N_2 reduction may be optimized for doped transition-metal nitrides by targeting properties intermediate to those of Mn and Fe, that is, an N_dE_d of about −50 eV. Since the correlation of d-state occupancy and nitride reactivity is linked through the stability of the metal–nitrogen bond, for a ternary system N_dE_d may be defined in first approximation as the arithmetic average of the value for the metals that form metal–nitrogen bonds.

Instead, the yield of NH_3 could be increased with a material that facilitates exergonic NH_3 evolution *via* metal nitride oxidation at low temperatures and exergonic N_2 reduction at higher temperatures. We suggest that this can be achieved by partially substituting the lattice nitrogen with hydrogen, as we examine for the reaction:

$$M_aN_bH_c + \frac{(3\delta+\varepsilon)}{2}H_2 \leftrightarrow M_aN_{b-\delta}H_{c+\varepsilon} + \delta NH_3 \quad (3)$$

where c is a stoichiometric constant and ε is the amount of incorporated lattice hydrogen. Fig. 1B shows an analogous plot for this reaction and suggests that the substitution of the nitrogen vacancies with hydrogen yields NH_3 exergonically at relatively low temperatures. The closing of the cycle:

$$M_aN_{b-\delta}H_{c+\varepsilon} + \frac{\delta}{2}N_2 \leftrightarrow M_aN_bH_c + \frac{\varepsilon}{2}H_2 \quad (4)$$

now has a negative slope – making it exergonic at elevated temperatures – since the evolution of H_2 is entropically favored at elevated temperatures. This feature theoretically circumvents the limited activities of typical Haber–Bosch catalysts due to scaling of the adsorption energies of nitrogen-containing surface species and the activation energy for the N_2 dissociation. This may be achieved using a metal nitride that liberates NH_3 *via* oxidative hydrogenation with H_2 at relatively low temperatures. The chemical potential of the nitride is thereafter re-established *via* reductive N_2 dissociation at ambient pressure and moderately elevated temperatures. In these materials M is an alkali or alkaline earth metal, and thus we see a correlation with the bonding valance s-electrons in the metal ground state, shown with Fig. 2B. The data indicates that the average energy of the s-states, *i.e.*, the s-band center, can be employed as an approximate descriptor of the reactivity of complex metal nitrides that allow for hydrogen intercalation. We note the deviation of Li-based materials from the correlation of the alkaline earth metal-based compounds can be understood due to the alkali-nature of Li. Generally, such incorporation of

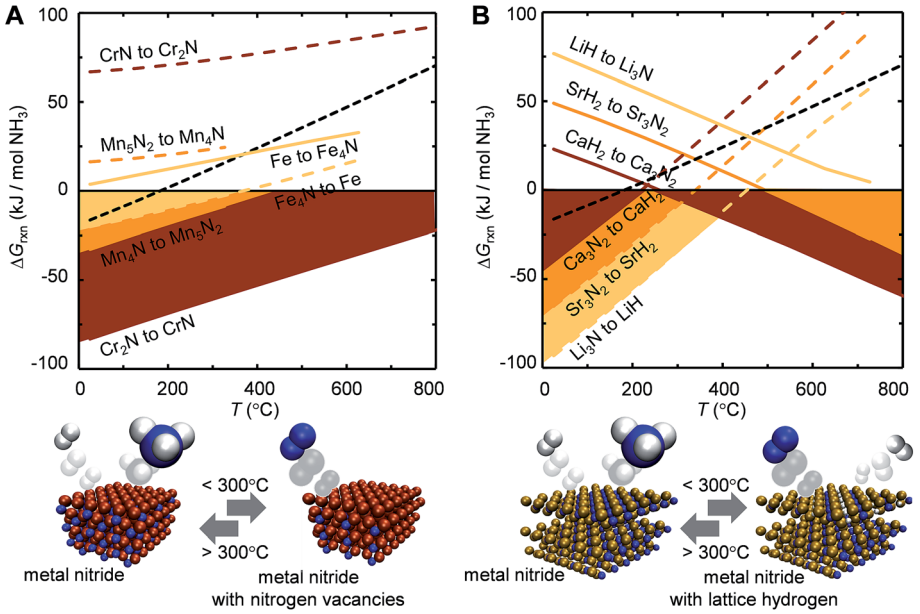

Fig. 1 Ammonia synthesis at 1 bar and up to 800 °C (computed from tabulated free energy data)[51] *via* (A) metal nitride reduction with H_2 (eqn (1), dashed lines) and N_2 reduction with reduced metal nitrides (eqn (2), solid lines) and (B) metal nitride hydrogenation (eqn (3), dashed line) and N_2 reduction with metal hydrides (eqn (4), solid line). Shaded regions mark exergonic reactions. The equilibrium of NH_3 with $3/2H_2$ and $1/2N_2$ is shown as reference at 1 bar (dotted line; negative values corresponding to NH_3 evolution).

hydrogen into the solid is desirable for a solar-driven thermochemical ammonia synthesis as it enables lower temperature ammonia evolution.

2.2 Formation of nitrogen vacancies *vs.* lattice hydrogen

This Section uses electronic structure calculations to outline how nitrogen vacancies control the intercalation of hydrogen and the evolution of NH_3, focusing on the (0001) surfaces of Mn_2N and Sr_2N. To quantify the reactivity of these materials, Table 1 shows free energy changes for key vacancy and surface reactions. We can see a net-energy penalty for forming surface and bulk nitrogen vacancies that is by more than 1 eV higher for $Sr_2N(0001)$ than for $Mn_2N(0001)$. The energy penalty for the nitrogen vacancy migration into the bulk, *i.e.*, $\Delta G_{vac,\ bulk} - \Delta G_{vac}$, is about equal. This suggests that the nitrogen vacancies of $Sr_2N(0001)$ require more energy to be formed and are more reactive than those of $Mn_2N(0001)$. This is a first indicator for the trend of surface adsorbates such as H* to fill vacancies. The strong hydrogen binding indicates that in the presence of H_2 both surfaces are expectedly covered with H*.

To understand the reaction mechanism of the lattice nitrogen with surface hydrogen, Fig. 3A and B show the energetics of forming 1/4 ML v_N at $Mn_2N(0001)$ and $Sr_2N(0001)$ yielding NH_x^* ($x = 0$, 1, 2 or 3) from surface hydrogen (and partly H_2 gas, in cases where 1 ML H* does not supply enough hydrogen to yield a specific H^*/NH_x^* surface coverage). The analysis points out a few general trends: the conversion of

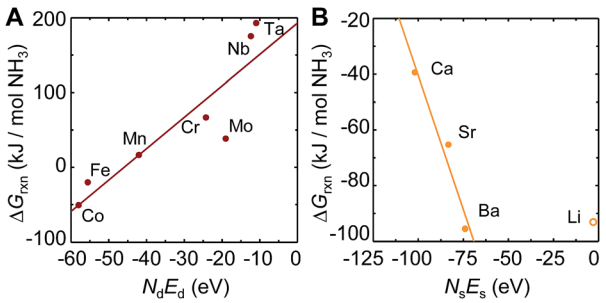

Fig. 2 Scaling of the free energy of the NH_3 evolution at 25 °C (computed from tabulated free energy data as described in Section 3.1) *via* metal nitride (A) reduction and (B) hydrogenation with the product of the number of electrons in the metal ground state, *N*, and the energy of these electrons, *E*, in the (A) d-states and (B) s-states. The metal marks the metallic constituent of the composition given with ESI.† Solid lines are fits to the data shown with solid symbols.

Table 1 Theoretical reactivity of the (0001) surface

Energy (eV)	Reaction[a]	Mn_2N	Sr_2N
ΔG_{vac}	$N^s_{lat} + \frac{3}{2}H_2 = v^s_N + NH_3$	0.50	1.52
$\Delta G_{vac,\ bulk}$	$N^{ss}_{lat} + \frac{3}{2}H_2 = v^{ss}_N + NH_3$	0.82	1.88
$\Delta G_{ads}[H^*]$	$* + \frac{1}{2}H_2 = H^*$	−0.79	−0.45
$\Delta G_{ads}[2H^*]^b$	$2* + H_2 = 2H^*$	−1.30	−1.10
$\Delta G_{ads}[H_2O^*]$	$* + H_2O = H_2O^*$	—[c]	−0.64
$\Delta G_{ads}[OH^*]$	$* + H_2O = OH^* + \frac{1}{2}H_2$	−1.47	−2.20
$\Delta G_{ads}[OH^*, H^*]$	$2* + H_2O = OH^* + H^*$	−1.81	−2.73

[a] Lat, s, and ss mark the lattice nitrogen, surface and subsurface. [b] Dissociative hydrogen adsorption at increased surface coverage of 1/2 ML H*. [c] H_2O dissociated to OH* and H*.

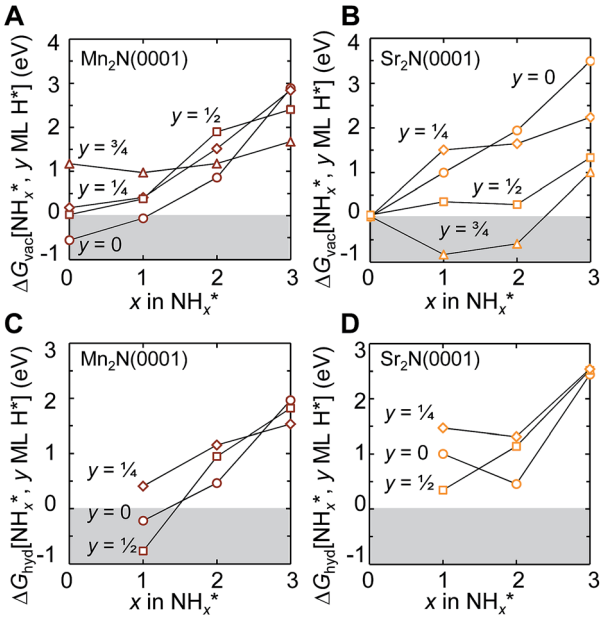

Fig. 3 Free energy diagrams for (A and B) forming 1/4 ML v_N yielding 1/4 ML NH_x^* and (C and D) hydrogenating NH_{x-1}^* to NH_x^* and y = 0 (circles), 1/4 (diamonds), 1/2 (squares), and 3/4 (triangles) ML H* adatoms on (A and C) $Mn_2N(0001)$ and (B and D) $Sr_2N(0001)$ at 25 °C and 1 bar. Lines are a guide only. The shaded regions mark energetically favourable surface reactions.

lattice nitrogen into v_N and N* is exergonic at $Mn_2N(0001)$ in the absence of H* and increasingly complicated in the presence of an increasing H* coverage. That is, H* appears to act as a surface "poison" for the adsorption of N* or NH* at $Mn_2N(0001)$. Second, while 1/4 ML N* is not formed on $Sr_2N(0001)$ with 1/4 ML v_N, which is independent of the H* coverage (±0.04 eV), the formation of v_N at $Sr_2N(0001)$ is more favorable if the lattice nitrogen yields NH* or NH_2^* in presence of 1/2–3/4 ML H* relative to 0–1/4 ML H*. That is, H* prevents the filling of v_N at $Sr_2N(0001)$ by surface nitrogen. Such energetic promotion of the vacancy formation by H* co-adsorbates is absent at $Mn_2N(0001)$ where H* mostly hinders formation of NH_x^* with x = 0, 1 or 2. We note the endergonic formation of NH_3^* that is stabilized by H* at both surfaces indicates that the direct formation of 1/4 ML NH_3^* from lattice nitrogen and 3/4 ML H* is unlikely. Furthermore, departures and "crossover" from these free energy trends are due to the source of the hydrogen and the rearrangement of adsorbates (ESI†).

Fig. 3C and D show the energy required to hydrogenate adsorbed nitrogen, which indicates a similar trend: the higher the degree of under-coordination of the adsorbed nitrogen at the surface the easier it is to hydrogenate the nitrogen, which involves breaking surface-nitrogen bonds. Fig. 4 shows that these bonds are favorably formed at three-fold metal sites with charge localization between the adsorbate and the nitrogen vacancy. This is opposed, for instance, to three clearly defined metal–carbon bonds for C* adsorbates at $Mo_2C(001)$.[9] The most notable exception from this trend is the highly unfavorable hydrogenation of N* to NH* at low H* coverage on $Sr_2N(0001)$ which is discussed in the following.

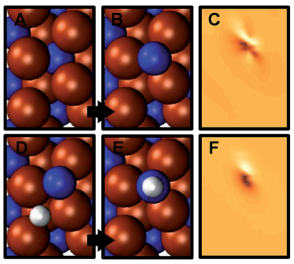

Fig. 4 Charge density differences (C and F), in units of the elementary charge per Å^3 at the height of the adsorbate N nucleus, between (B) N* at $Mn_2N(0001)$ with 1/4 ML v_N and (A) the stoichiometric surface and the balance N, and for the hydrogenation of (D) 1/4 ML N* to (E) NH*.

The optimized adsorption geometries are given with Fig. 5. The figure shows intercalation of hydrogen at $Sr_2N(0001)$ that is not observed at $Mn_2N(0001)$. In absence of surface hydrogen, the strong Sr–N bonds result in unstable 1/4 ML N* that is filling the vacancies at $Sr_2N(0001)$, which is visualized by the identical geometries shown with panels (2a and 2b) of Fig. 5, while $Mn_2N(0001)$ yields a stable 1/4 ML N* surface coverage (Fig. 5, panels 1a and 1b). In presence of surface hydrogen, Fig. 5 shows that the energetic promotion of forming 1/4 ML v_N and NH* or NH_2* at high H* coverage at $Sr_2N(0001)$ but not at $Mn_2N(0001)$ (shown with Fig. 3A and B) is due to filling of v_N by H* yielding lattice hydrogen at $Sr_2N(0001)$ (Fig. 5, panels 2c and 2d *vs.* 1c and 1d). These calculations show hydrogen intercalating at the surface. The tendency of this lattice hydrogen to diffuse further into the bulk leading to formation of hydrides is outlined in Section 2.1. Finally, hydrogenating 1/4 ML N* with H* to NH* is energetically demanding at $Sr_2N(0001)$ relative to $Mn_2N(0001)$ (Fig. 3C and D) since it requires formation of 1/4 ML v_N at $Sr_2N(0001)$ (Fig. 5, panels 2e and 2f *vs.* 1e and 1f).

In summary, the lattice nitrogen activity was outlined to control the formation and hydrogenation of adsorbed nitrogen and the formation of lattice hydrogen. These trends are analogous to the reactivity of the bulk metal nitrides.

2.3 Ammonia from partial reduction of metal nitrides

In the following two Sections we study the role of nitrogen vacancies experimentally by comparing the reactivity of Mn-based transition-metal nitrides to the reactivity of Ca- and Sr-based alkaline earth metal nitrides. This Section characterizes the NH_3 evolution *via* the reduction of manganese nitride.

Fig. 6A shows the evolution of ammonia from the reaction of manganese nitride with H_2. The yield of NH_3 relative to the lattice nitrogen available for the reaction was at maximum ~8 mol% NH_3 after 60 min at 700 °C. The location of the optimum at an intermediate temperature is presumably due to slow reaction kinetics at lower temperatures and thermal decomposition of NH_3 at higher temperatures. At low NH_3 yields we observe decreasing NH_3 yields with time, which is presumably due to partial stripping of NH_3 with the H_2 routed through the liquid absorbent. Since we observe this effect only for NH_3 yields between 10^{-5} to 3×10^{-3}, NH_3 stripping is assumed to not significantly affect NH_3 evolution with higher yields above

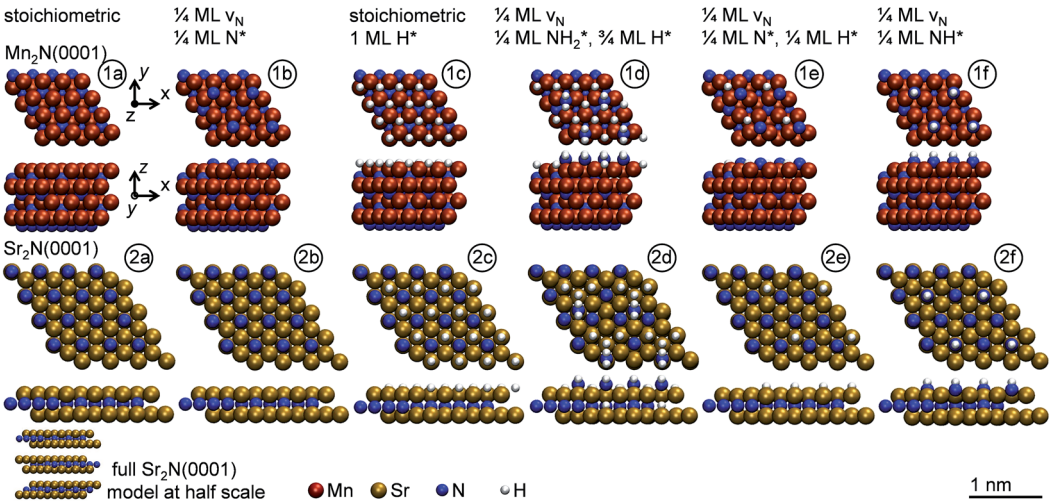

Fig. 5 Optimized adsorption geometries for the indicated surface conditions (top two lines) of (1a to 1f) $Mn_2N(0001)$ and (2a to 2f) $Sr_2N(0001)$. The view along the *y*-axis of the $Sr_2N(0001)$ model is limited to the upper layer.

300 °C. More important, the ammonia evolution at 550 and 700 °C is described best by a reaction- or gas diffusion-limited kinetic model with an activation energy estimated from an Arrhenius plot of 98 ± 7 kJ mol^{-1}. This indicates that the kinetics of the NH_3 formation with H_2 are more sensitive to temperature than the steam hydrolysis of Mn_4N with an activation energy of 63 kJ mol^{-1}, where oxygen intercalation fills the nitrogen vacancies.[34]

Fig. 6B shows the composition of the solid after the reaction with H_2. Increasing temperature decreases the fraction of $Mn_6N_{2.58}$ and yields a maximum Mn_4N fraction near 700 °C. This suggests that NH_3 is formed through the reduction of a higher nitride into a lower nitride phase that contains less nitrogen and that decomposes thermally at 1000 °C to Mn and N_2.[51] The thickness of the reaction front through a particle with constant volume (*i.e.*, $L = X_N \rho_{nitride}^{-1} A_{BET}^{-1}$, where $\rho_{nitride}$ is the density of the reacting nitride and X_N is the fraction of liberated lattice nitrogen), can be estimated based on a nitrogen mass balance to be 54 nm or 46 nm for NH_3 evolution at 700 °C from $Mn_6N_{2.58}$ or Mn_4N, respectively. Fig. 6 suggests that this bulk reaction is limited at the surface: by gas-phase diffusion or the surface reaction, that is by the formation of nitrogen vacancies and the hydrogenation of surface nitrogen. We note, attempting to control the lattice nitrogen reactivity *via* doping Mn_4N with Fe did not increase the NH_3 evolution at 700 °C (ESI†), which may be due to the catalytic activity of Fe in establishing the chemical equilibrium in NH_3, N_2 and H_2 gas mixtures.[4]

For comparison, some metal nitrides that cannot be regenerated with 1 bar N_2 may yield significant quantities of NH_3. Ni_3N, Cu_3N, Zn_3N_2 and Ta_3N_5 may liberate 30, 25, 23, and 13 mol% of their lattice nitrogen as NH_3 when reacted for at least 30 min at 250, 250, 400, and 700 °C, respectively.[46] Ammonia yields decrease when reacting H_2 with more stable nitrides: such as to 8 mol% with Co_3Mo_3N for 60 min at 400 °C.[44] Manganese nitrides can be formed from N_2 at 1 bar, as shown with Fig. 1A, and spent iron-doped manganese nitrides can be regenerated with N_2, as shown for three consecutive cycles with Fig. S3.† However, stable performance and long-term stability of metal nitrides, in form of pellets or porous structures for instance,[31,33,37] have to be assessed in the future.

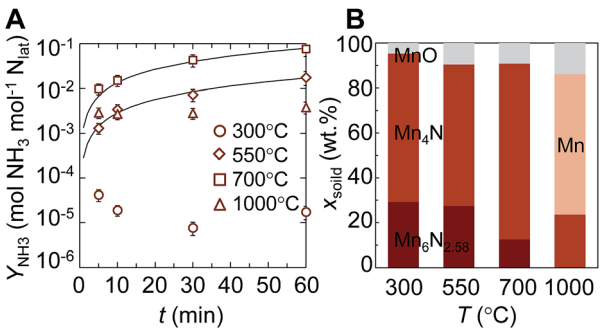

Fig. 6 NH_3 evolution *via* isothermal transition-metal nitride reduction: (A) NH_3 yield *vs.* time and (B) solid weight fractions from the reaction of Mn_4N with H_2 at 1 bar *vs.* temperature. Error bars are *via* error propagation within a 95% confidence interval. Solid lines are shrinking-core models for the data at 550 °C and 700 °C controlled by the chemical reaction or gas phase diffusion.

2.4 Ammonia from formation of hydrogenated metal nitrides

Some alkali and alkaline earth metal nitrides may yield ammonia exergonically from the reaction with H_2 due to the intercalation of hydrogen, as discussed in Section 2.1. The electronic structure calculations reported in Section 2.2 outline how the reactivity of the bulk metal nitrides correlates with the activity of the nitrogen vacancies. With the experimental results in this Section we show the ready evolution of ammonia and the corresponding hydrogenated metal compounds from the nitrides of Ca and Sr under H_2.

The liberation of the lattice nitrogen of Ca_3N_2 and Sr_2N as NH_3 may be limited kinetically at the low temperatures that are favored thermodynamically, as was shown with Fig. 1.

Therefore, Ca_3N_2 and Sr_2N, as well as $Mn_6N_{2.58}$ as reference, were reacted with H_2 at 1 bar and a range of temperatures including the low and high end of the spectrum, 220–850 °C. Fig. 7A shows the NH_3 yield over the course of three heating cycles. Sr_2N liberates NH_3 nearly instantaneously during the initial heating period, which is followed by a continuous and comparably slight increase of the NH_3 yield. The absolute NH_3 yield from Ca_3N_2 is lower than that from Sr_2N, but both alkaline earth metal nitrides liberate NH_3 faster and in significantly larger quantities than the transition-metal nitride.

The minimum apparent reaction rates of hydrogenating lattice nitrogen with H_2 into NH_3 are estimated with 0.9 ± 0.2, 1.3 ± 0.4 and 2.1 ± 0.2 μmol NH_3 (mol metal × s)$^{-1}$ for $Mn_6N_{2.58}$, Ca_3N_2 and Sr_2N respectively. Since OH and H_2O adsorb strongly at alkaline earth metal nitrides (Table 1), this is accounting for partial nitride hydrolysis by traces of adsorbed water, although neither Sr_2N nor Ca_3N_2 appeared visually oxidized after the reaction. These reaction rates of Ca_3N_2 and Sr_2N and significant formation of up to 12 mol% NH_3 from Ca_3N_2 that we observed with a late onset between 30–60 min heating at various H_2 flow rates (ESI†) indicate that NH_3 is formed from the reaction of lattice nitrogen and H_2. For comparison, these yields are higher than the previously reported 1 mol% NH_3 from Ca_3N_2 heated for 120 min at 800 °C in H_2, which can be understood due to the unfavorable NH_3–N_2/H_2 equilibrium that is established during these early studies by F. Haber, *et al.*[50]

The intercalation of hydrogen can be observed for Ca_3N_2 yielding mainly Ca_2NH and Sr_2N yielding SrH_2: Fig. 7B shows the composition of Ca_3N_2, determined *via* XRD, after the reaction with H_2. Increasing temperature increases the formation of Ca_2NH, with nominally 25 mol% lattice hydrogen. From the yield of Ca_2NH, the activation energy of the NH_3 evolution is about 42 ± 7 kJ mol^{-1}. However, the different surface morphologies, shown with Fig. 8, and the slightly different BET surface areas, given with Table S1 (ESI†), of the nitrides indicate that this value of the activation energy cannot be compared directly to the activation energy of the NH_3 evolution from manganese nitride, given in Section 2.3. The lower activation energy of Ca_3N_2 is, however, qualitatively in agreement with the higher NH_3 evolution rate with Ca_3N_2, relative to $Mn_6N_{2.58}$. Furthermore, a 58% higher NH_3 evolution rate from Sr_2N with a 16% lower specific surface area relative to Ca_3N_2 indicates that the reported results are not solely due to the available surface area. These results confirm that the intercalation of the two alkaline earth metal nitrides by hydrogen promotes the ammonia evolution from the lattice nitrogen at the surface.

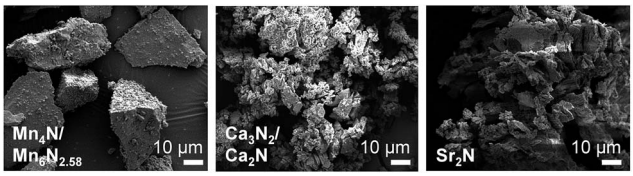

Fig. 8 Scanning electron micrographs of the metal nitrides.

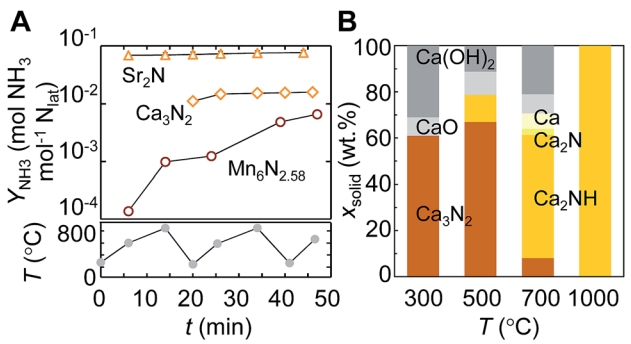

Fig. 7 NH_3 evolution *via* metal nitride hydrogenation at various temperatures: (A) NH_3 yield *vs.* time (arithmetic average of three experiments) from the reactions of Ca_3N_2, Sr_2N, and $Mn_6N_{2.58}$ with H_2 at 1 bar, shown on the upper panel, and the corresponding temperature profile, on the lower panel; (B) weight fraction of Ca_3N_2 heated for 60 min under H_2 (XRD analyses in air). Error bars are *via* error propagation within a 95% confidence interval. Solid lines are a guide only.

3. Methods

3.1 Thermochemical equilibrium calculations

To guide the design of looped metal nitride catalysts, the thermochemical equilibrium of various bulk metal nitrides, H_2, and their reaction products was determined at 1 bar and as a function of temperature from tabulated free energy data.[51] Per convention, negative free energy differences mark exergonic reactions.

3.2 Electronic structure calculations

To determine the NH_3-evolution-controlling mechanism at the atomic scale, hexagonal ζ-Mn_2N and trigonal Sr_2N were modeled *via* density functional theory (DFT), performed with the open-source planewave pseudopotential periodic electronic-structure code DACAPO.[53–55] Atomic manipulations were handled in the Atomic Simulation Environment (ASE)[56] and exchange–correlation interactions were treated by the revised Perdew–Burke–Ernzerhof (RPBE) functional of Hammer, Hansen, and Nørskov[57] derived in the generalized gradient approximation (GGA). A **k**-point sampling of 4 × 4 × 4 for bulk and 4 × 4 × 1 for surface calculations was used for sampling of the Brillouin zone in the *x*, *y* and *z* directions, with the *z* direction orthogonal to the surface slab. A Fermi-Dirac smearing of 0.1 eV was used to achieve convergence and results were extrapolated to 0 K. The linesearch BFGS algorithm was employed for relaxing atomic geometries until the maximum force on any unconstrained atom was less than 0.05 eV Å^{-1}. To avoid reminiscent stress in the calculations, the lattice constants were chosen as the DFT-calculated lattice constants (*i.e.*, (*a*, *c*) = (2.81, 4.44) Å for Mn_2N, and (3.90, 21.15) Å for Sr_2N), which are within 2.2% of the experimental values (*i.e.*, (*a*, *c*) = (2.84, 4.51) Å for Mn_2N,[58] and (3.86, 20.70) Å for Sr_2N[59]). Calculations for Mn_2N were spin-polarized. All surface calculations were performed for the (0001) facet with 2 × 2 × 4 or 2 × 2 × 6 metal atoms in the *x*, *y* and *z* directions of the Mn_2N or Sr_2N slab. The surfaces were modeled with 10 Å of vacuum perpendicular to the surface with the lower layers of the slab constrained to the

bulk geometry while the atoms in the upper two layers were always optimized to zero-force positions. The interaction between the dipole moments of surfaces was decoupled *via* introduction of a dipole layer in the vacuum.

The correlated electronic structure of certain metal oxides is not well described with simple GGA methods. This is sometimes addressed by the inclusion of an empirical Hubbard U term that accounts for on-site Coulomb repulsion and exchange interactions, thereby correcting self-interaction errors, when modeling certain metal oxides,[60–62] while other metal oxides have been modeled well without the additional U parameter[63] (and references therein). The value of U can be determined self-consistently,[62] however, commonly it is chosen by fitting the experimental band gap[60] or reaction energetics (resulting in a consistent offset of the free energy of reaction with varying U).[64] Introducing nitrogen into a transition metal lattice may lead to partial electron localization with a minor increase in the metal oxidation state, compared to the presence of lattice oxygen.[65] Hence, transition metal nitrides, including Mn_2N, are typically modeled without a Hubbard U correction.[23,66] Verifying this and assessing the use of GGA + U methods for metal nitride surfaces is an important point. In a prospective article, we will show how adsorption energies respond to the value of U only for metal compounds that possess a (pseudo) band gap. While Sr_2N and Mn_2N are metallic conductors,[58,59] Sr_2N exhibits localized N 2p states.[67] Thus, whether GGA + U methods may improve the accuracy of DFT-computed adsorption energies at Sr_2N surfaces deserves further study.

To aid in our description of nitride activity from first principles, four free-energies are defined. First, ΔG_{vac} is the free energy required to form a nitrogen vacancy, v_N, at the surface:

$$\Delta G_{vac} \equiv G_s[v_N] - (G_s - G_N^r) \quad (5)$$

where G_s is the free energy of the intact surface, $G_s[v_N]$ is the free energy of the surface with 1/4 monolayer (ML, relative to the number of surface metal atoms) v_N and G_N^r is the reference energy of nitrogen in the gas phase, respectively.

Next, $\Delta G_{ads}[A^*]$ is the adsorption energy of the adsorbate(s) A (an asterisk indicates an adsorbed species):

$$\Delta G_{ads}[A^*] \equiv G_s[A^*] - (G_s + G_A^r) \quad (6)$$

where $G_s[A^*]$ is the free energy of the surface with the adsorbate(s) and G_A^r the free energy of the reference adsorbate(s).

Third, $\Delta G_{vac}[NH_x^*, yH^*]$ is the free energy change to create adsorbed NH_x species while creating nitrogen vacancies and leaving y adsorbed H's at the surface; that is to form 1/4 ML v_N at a surface with z ML H* ($z = 0$, 1/4, 1/2, 3/4 or 1) yielding 1/4 ML NH_x^* ($x = 0$, 1, 2 or 3, corresponding to 0, 1/4, 1/2 or 3/4 ML H*) and y ML H* remaining at the surface ($y = 0$, 1/4, 1/2 or 3/4):

$$\Delta G_{vac}[NH_x^*, yH^*] \equiv G_s[v_N, NH_x^*, yH^*] - (G_s[zH^*] + (x + y - z)G_H^r) \quad (7)$$

where $G_s[v_N, NH_x^*, yH^*]$, $G_s[zH^*]$ and G_H^r are the energy of the surface after or before the formation of v_N and the reference energy of the balance hydrogen gas.

Finally, $\Delta G_{hyd}[NH_x^*, yH^*]$ is the energy for hydrogenating NH_{x-1}^* with $(y + 1)$ pre-adsorbed H*, leaving NH_x^* and yH*:

$$\Delta G_{hyd}[NH_x^*, yH^*] \equiv G_s[v_N, NH_x^*, yH^*] - G_s[v_N, NH_{x-1}^*, (y + 1)H^*] \quad (8)$$

where $G_s[v_N, NH_{x-1}^*, (y + 1)H^*]$ is the energy of the surface before the hydrogenation.

Details on the local optimization procedures, references energies, conversion of electronic energies to free energies, and adsorption energetics in presence of OH and H_2O and at oxynitride surfaces are given with ESI.†

3.3 Metal nitride preparation

Manganese was nitridated[34] by heating 2 g Mn in N_2 under two different thermal conditions; first, for 120 min at 700 °C which yielded 59–67 wt% ε-Mn_4N and 25–34 wt% ζ-$Mn_6N_{2.58}$ (denoted as Mn_4N), and second, for 240 min at 750 °C which yielded 91–94 wt% ζ-$Mn_6N_{2.58}$ (denoted as $Mn_6N_{2.58}$). We note ζ-phase manganese nitride ranges from 28.6–33.3 mol% lattice nitrogen including Mn_5N_2, $Mn_6N_{2.58}$, and Mn_2N.[58] The nitride characterization is summarized with Table S1 (ESI†). Fe-doped Mn nitride, Fe/Mn_4N, was prepared by heating 2 g of an equimolar mixture Mn and Fe powder for 120 min in N_2 yielding 26 ± 1 wt% ε-Mn_4N and 16 ± 1 wt% ζ-$Mn_6N_{2.58}$. All Mn-containing powders were pretreated at 60 °C for 10 min in air to remove water. Ca_3N_2 and Sr_2N[34,68] were prepared by heating 4.4 g metal pieces for 240 min (Ca) or 420 min (Sr) in N_2 and milling for about 5 min with mortar and pestle. The fraction of hydroxides formed when handling Ca_3N_2 or Sr_2N during the X-ray diffraction (XRD) analysis in air were disregarded in NH_3 yield calculations since these materials were otherwise handled in Ar. All N_2 flows were 1.9 ± 0.1 $L_{(STP)}$ N_2 min^{-1}.

3.4 Reduction of Mn_4N and $Mn_6N_{2.58}$ with H_2

To probe the reactivity of manganese nitride, 651 ± 2 mg Mn_4N containing 3.01 ± 0.01 mmol lattice nitrogen was heated in a quartz boat with a tube furnace at ambient pressure. The tube furnace was a HTF55347C model, Lindberg/Blue, with a quartz tube that was purged before each experiment for 10 min with N_2 to remove residual O_2 and H_2O. The temperature was ramped from 100 to 300 °C or from 400 to 550, 700 and 1000 °C respectively. H_2 was supplied at 0.5 ± 0.1 $L_{(STP)}$ H_2 min^{-1} and final temperatures were held for 60 min. The gas leaving the furnace was routed through a liquid absorbent consisting of 50 ± 5 $mL_{(STP)}$ 10 mM HCl, chilled with ice-cold H_2O. Five mL samples were taken at 0, 5, 10, 30 and 60 ± 0.5 min after the reaction temperature was reached. These samples were analyzed for NH_3 as described below. After 60 min the furnace was cooled to below 100 °C. Solids were stored at 4 °C. All liquids were stored at room temperature. Additionally, the NH_3 evolution from Fe-doped Mn_4N was quantified (ESI†).

3.5 Hydrogenation of Ca_3N_2 and Sr_2N with H_2

The optimum temperature for reacting Ca_3N_2 with 0.5 ± 0.1 $L_{(STP)}$ H_2 min^{-1} was determined using the experimental setup

described in Section 3.4 without the absorption vessel. The powder (476 ± 170 mg, *i.e.*, 6 ± 2 mmol lattice nitrogen) was held for 60 min at 300, 500, 700 and 1000 °C and analyzed for the loss of lattice nitrogen. All Ca-containing solids were stored under Ar at 4 °C. The effect of the H_2 flow rate on the NH_3 yield from Ca_3N_2 was tested (ESI†). To compare the NH_3 evolution kinetics between metal nitride reduction ($Mn_6N_{2.58}$) and hydrogenation (Ca_3N_2 and Sr_2N), 519 ± 18 mg metal nitride (2.8–7.0 mmol lattice nitrogen) were heated in 0.5 ± 0.1 $L_{(STP)}$ H_2 min^{-1} from 220 to 850 ± 5 °C. After holding temperatures for 2 min, the furnace was cooled to 250 °C. The temperature change was repeated in triplicate. Liquid samples were taken at 250, 550 and 850 °C while the solids were analyzed after three cycles, reintroduced into the furnace, heated for 120 min at 750 °C in 1.9 ± 0.1 $L_{(STP)}$ N_2 min^{-1} and analyzed anew.

3.6 Analytical

Solids were weighed (AE260 DeltaRange balance, ±0.1 mg, Mettler) and analyzed *via* XRD (Miniflex II diffractometer, Cu-target X-ray tube, Rigaku, 5–80° 2θ range, 1 or 10° 2θ per min scan speed, PDXL Software Version 1.6.0.0 for quantitative solid phase analysis). The XRD analysis was in air which explains minor metal oxide and hydroxide fractions. To confirm N_2 reduction energy-dispersive X-ray spectroscopy (EDS) was employed using a S-3500N scanning electron microscope (SEM, 20 keV, Hitachi; Link Pentafet 7021 X-ray detector and Inca Energy X-ray analysis software, both Oxford Instruments). The specific BET surface area, A_{BET}, was analyzed using N_2 at NanoScale Inc., Manhattan, KS. NH_3 was quantified with an NH_3 Ion Selective Electrode and a pH/ISE Controller model 270 (both Denver Instrument). The concentration of dissolved NH_3 was estimated with zeroing for the signal from pure water. As estimated from the pH change, the formation of N_2H_4 was negligible relative to NH_3 formation in all reported experiments. The outlet of the absorption vessel was equipped with an NH_3 gas detection tube (0.25–3 or 5–70 ppm NH_3 detection range, Dräger). Ammonia yield, Y_{NH_3}, is reported as the molar ratio of NH_3 captured by the absorbent at a given time relative to the lattice nitrogen stored in the solid initially. The data is fitted to a kinetic model limited by the reaction or gas phase diffusion (ESI†).

3.7 Chemicals

Mn (99.9%, −325 mesh) and Fe (99.9%, −325 mesh) were from Noah Technologies, Ca (99%, granular) and NH_4Cl (99.5%) were from Acros, Sr (99%, pieces) was from MP Biomedicals and NaOH (99.6%, pellets) and HCl (12.1 N) were from Fisher Scientific. H_2O was deionized (Direct-Q 3 UV, Millipore) and degassed with Ar. H_2, N_2 and Ar (all UHP Zero grade) were from Linweld.

4. Conclusions

We have introduced chemical looping of metal nitride catalysts for solar-driven synthesis of ammonia at ambient pressure from overall, water, N_2, and concentrated sunlight as source of renewable process heat. Augmented NH_3 evolution due to the formation of lattice hydrogen was correlated to the exergonic character of the hydrogenation of alkali and alkaline earth metal nitrides *vs.* endergonic reduction of transition-metal nitrides. These trends were confirmed experimentally and rationalized *via* electronic structure calculations which showed that the lattice nitrogen activity controls hydrogen intercalation and the energetics of forming and hydrogenating adsorbed nitrogen. The energy of the metal d-states was discussed as a quantitative descriptor for the design of ternary metal nitrides with reactivities between those of Fe- and Mn-based nitrides, while the energy of the metal s-states may guide the design of, for instance Li-doped, alkaline earth metal nitrides for an NH_3 evolution promoted by the intercalation of surface hydrogen. Stable NH_3 evolution and long-term mechanical stability of metal nitride catalysts, in form of pellets or porous ceramics for instance, have to be assessed in the future.

Acknowledgements

Kent E. Hampton is acknowledged for his technical assistance. All glass and quartz ware manufactured at Kansas State University was from James R. Hodgson. The experimental components are based upon work supported by National Science Foundation Grant # 0903701: "Integrating the Socio-economic, Technical, and Agricultural Aspects of Renewable and Sustainable Biorefining Program, awarded to Kansas State University." Funding by the Center for Sustainable Energy, Kansas State University is kindly acknowledged. The theoretical calculations and analysis were supported by the Office of Naval Research (Young Investigator Award N00014-12-1-0851). Electronic structure calculations were conducted at the Center for Computation and Visualization, Brown University.

Notes and references

1 I. Rafiqul, C. Weber, B. Lehmann and A. Voss, *Energy*, 2005, **30**, 2487–2504.
2 V. Smil, *Enriching the Earth: Fritz Haber, Carl Bosch, and the Transformation of World Food Production*, The MIT Press, Cambridge, Massachusetts, 2004.
3 V. Smil, *Nature*, 1999, **400**, 415.
4 G. Ertl, *Angew. Chem., Int. Ed.*, 2008, **47**, 3524–3535.
5 Z. Kirova-Yordanova, *Energy*, 2004, **29**, 2373–2384.
6 S. K. Ritter, *Chem. Eng. News*, 2008, **86**, 53.
7 A. Vojvodic, A. J. Medford, F. Studt, F. Abild-Pedersen, T. S. Khan, T. Bligaard and J. K. Nørskov, *Chem. Phys. Lett.*, 2014, **598**, 108–112.
8 F. Abild-Pedersen, J. Greeley, F. Studt, J. Rossmeisl, T. R. Munter, P. G. Moses, E. Skúlason, T. Bligaard and J. K. Nørskov, *Phys. Rev. Lett.*, 2007, **99**, 016105.
9 R. Michalsky, Y.-J. Zhang, A. J. Medford and A. A. Peterson, *J. Phys. Chem. C*, 2014, **118**, 13026–13034.
10 A. Klerke, C. H. Christensen, J. K. Nørskov and T. Vegge, *J. Mater. Chem.*, 2008, **18**, 2304–2310.
11 C. H. Christensen, T. Johannessen, R. Z. Sørensen and J. K. Nørskov, *Catal. Today*, 2006, **111**, 140–144.
12 C. W. Gross and S. C. Kong, *Fuel*, 2013, **103**, 1069–1079.

13 http://nh3fuelassociation.org/2013/06/20/the-amveh-an-ammonia-fueled-car-from-south-korea/(retrieved 5/2/14).
14 A. J. Reiter and S.-C. Kong, *Energy Fuels*, 2008, **22**, 2963–2971.
15 F. Vitse, M. Cooper and G. G. Botte, *J. Power Sources*, 2005, **142**, 18–26.
16 J. C. Ganley, *J. Power Sources*, 2008, **178**, 44–47.
17 S. Dahl and I. Chorkendorff, *Nat. Mater.*, 2012, **11**, 100–101.
18 M. Carmo, D. L. Fritz, J. Merge and D. Stolten, *Int. J. Hydrogen Energy*, 2013, **38**, 4901–4934.
19 G. P. Van der Laan and A. Beenackers, *Catal. Rev.: Sci. Eng.*, 1999, **41**, 255–318.
20 V. Kordali, G. Kyriacou and C. Lambrou, *Chem. Commun.*, 2000, 1673–1674.
21 E. Skúlason, T. Bligaard, S. Gudmundsdóttir, F. Studt, J. Rossmeisl, F. Abild-Pedersen, T. Vegge, H. Jónsson and J. K. Nørskov, *Phys. Chem. Chem. Phys.*, 2012, **14**, 1235–1245.
22 G. Marnellos and M. Stoukides, *Science*, 1998, **282**, 98–100.
23 J. G. Howalt and T. Vegge, *Phys. Chem. Chem. Phys.*, 2013, **15**, 20957–20965.
24 Y. Abghoui, A. L. Garden, V. F. Hlynsson, S. Björgvinsdóttir, H. Ólafsdóttir and E. Skúlason, *Phys. Chem. Chem. Phys.*, 2015, **17**, 4909–4918.
25 R. Lan, J. T. S. Irvine and S. W. Tao, *Sci. Rep.*, 2013, **3**, 1145.
26 R. Michalsky, B. J. Parman, V. Amanor-Boadu and P. H. Pfromm, *Energy*, 2012, **42**, 251–260.
27 M. E. Gálvez, A. Frei, M. Halmann and A. Steinfeld, *Ind. Eng. Chem. Res.*, 2007, **46**, 2047–2053.
28 R. Michalsky and P. H. Pfromm, *AIChE J.*, 2012, **58**, 3203–3213.
29 R. Michalsky and P. H. Pfromm, *Sol. Energy*, 2011, **85**, 2642–2654.
30 K. M. Allen, N. Auyeung, N. Rahmatian, J. F. Klausner and E. N. Coker, *JOM*, 2013, **65**, 1682–1693.
31 P. Furler, J. Scheffe, M. Gorbar, L. Moes, U. Vogt and A. Steinfeld, *Energy Fuels*, 2012, **26**, 7051–7059.
32 W. Villasmil, M. Brkic, D. Wuillemin, A. Meier and A. Steinfeld, *J. Sol. Energy Eng.*, 2014, **136**, 011017.
33 M. Romero and A. Steinfeld, *Energy Environ. Sci.*, 2012, **5**, 9234–9245.
34 R. Michalsky and P. H. Pfromm, *J. Phys. Chem. C*, 2012, **116**, 23243–23251.
35 M. H. Yang, A. J. Allen, M. T. Nguyen, W. T. Ralston, M. J. MacLeod and F. J. DiSalvo, *J. Solid State Chem.*, 2013, **205**, 49–56.
36 C. Hargus, R. Michalsky and A. A. Peterson, *Energy Environ. Sci.*, 2014, **7**, 3122–3134.
37 W. C. Chueh, C. Falter, M. Abbott, D. Scipio, P. Furler, S. M. Haile and A. Steinfeld, *Science*, 2010, **330**, 1797–1801.
38 W. L. Zhu, R. Michalsky, O. Metin, H. F. Lv, S. J. Guo, C. J. Wright, X. L. Sun, A. A. Peterson and S. H. Sun, *J. Am. Chem. Soc.*, 2013, **135**, 16833–16836.
39 A. A. Peterson and J. K. Nørskov, *J. Phys. Chem. Lett.*, 2012, **3**, 251–258.
40 D. Friebel, V. Viswanathan, D. J. Miller, T. Anniyev, H. Ogasawara, A. H. Larsen, C. P. O'Grady, J. K. Nørskov and A. Nilsson, *J. Am. Chem. Soc.*, 2012, **134**, 9664–9671.
41 N. M. Marković and P. N. Ross, *Surf. Sci. Rep.*, 2002, **45**, 117–229.
42 C. Doornkamp and V. Ponec, *J. Mol. Catal. A: Chem.*, 2000, **162**, 19–32.
43 C. L. Muhich, B. W. Evanko, K. C. Weston, P. Lichty, X. H. Liang, J. Martinek, C. B. Musgrave and A. W. Weimer, *Science*, 2013, **341**, 540–542.
44 S. M. Hunter, D. McKay, R. J. Smith, J. S. J. Hargreaves and D. H. Gregory, *Chem. Mater.*, 2010, **22**, 2898–2907.
45 C. J. H. Jacobsen, S. Dahl, B. S. Clausen, S. Bahn, A. Logadottir and J. K. Nørskov, *J. Am. Chem. Soc.*, 2001, **123**, 8404–8405.
46 A. M. Alexander, J. S. J. Hargreaves and C. Mitchell, *Top. Catal.*, 2012, **55**, 1046–1053.
47 P. Chen, Z. T. Xiong, J. Z. Luo, J. Y. Lin and K. L. Tan, *Nature*, 2002, **420**, 302–304.
48 U. Ash-Kurlander, G. E. Shter, S. Kababya, A. Schmidt and G. S. Grader, *J. Phys. Chem. C*, 2013, **117**, 1237–1246.
49 D. E. Demirocak, S. S. Srinivasan, M. K. Ram, J. N. Kuhn, R. Muralidharan, X. Li, D. Y. Goswami and E. K. Stefanakos, *Int. J. Hydrogen Energy*, 2013, **38**, 10039–10049.
50 F. Haber and G. van Oordt, *Z. Anorg. Chem.*, 1905, **44**, 341–378.
51 I. Barin, *Thermochemical Data of Pure Substances*, VCH Verlagsgesellschaft mbH, Weinheim, Federal Republic of Germany, 1993, 0–6940.
52 B. Hammer and J. K. Nørskov, *Surf. Sci.*, 1995, **343**, 211–220.
53 D. Vanderbilt, *Phys. Rev. B: Condens. Matter Mater. Phys.*, 1990, **41**, 7892–7895.
54 M. C. Payne, M. P. Teter, D. C. Allan, T. A. Arias and J. D. Joannopoulos, *Rev. Mod. Phys.*, 1992, **64**, 1045–1097.
55 G. Kresse and J. Furthmüller, *Comput. Mater. Sci.*, 1996, **6**, 15–50.
56 S. R. Bahn and K. W. Jacobsen, *Comput. Sci. Eng.*, 2002, **4**, 56–66.
57 B. Hammer, L. B. Hansen and J. K. Nørskov, *Phys. Rev. B: Condens. Matter Mater. Phys.*, 1999, **59**, 7413–7421.
58 Y. J. Liu, L. M. Xu, X. Y. Li, P. Hu and S. W. Li, *J. Appl. Phys.*, 2010, **107**, 103914.
59 N. E. Brese and M. O'Keeffe, *J. Solid State Chem.*, 1990, **87**, 134–140.
60 Y. L. Lee, J. Kleis, J. Rossmeisl and D. Morgan, *Phys. Rev. B: Condens. Matter Mater. Phys.*, 2009, **80**, 224101.
61 H. J. Kulik and N. Marzari, *J. Chem. Phys.*, 2011, **134**, 094103.
62 M. Cococcioni and S. de Gironcoli, *Phys. Rev. B: Condens. Matter Mater. Phys.*, 2005, **71**, 035105.
63 R. Michalsky, A. Steinfeld, V. Botu, C. M. Hargus and A. A. Peterson, *Adv. Energy Mater.*, 2014, **4**, 1401082.
64 M. García-Mota, M. Bajdich, V. Viswanathan, A. Vojvodic, A. T. Bell and J. K. Nørskov, *J. Phys. Chem. C*, 2012, **116**, 21077–21082.
65 A.-M. Alexander and J. S. J. Hargreaves, *Chem. Soc. Rev.*, 2010, **39**, 4388–4401.
66 X. P. Du, V. C. Lo and Y. X. Wang, *J. Comput. Chem.*, 2012, **33**, 18–24.
67 C. M. Fang, G. A. de Wijs, R. A. de Groot, H. T. Hintzen and G. de With, *Chem. Mater.*, 2000, **12**, 1847–1852.
68 R. Chemnitzer, G. Auffermann, D. M. Többens and R. Kniep, *Z. Anorg. Allg. Chem.*, 2005, **631**, 1813–1817.

